Atmospheric Research 151 (2015) 2–19

Contents lists available at ScienceDirect

Atmospheric Research

journal homepage: www.elsevier.com/locate/atmos

A review on ice fog measurements and modeling

I. Gultepe [a,*], B. Zhou [b,c], J. Milbrandt [d], A. Bott [e], Y. Li [f], A.J. Heymsfield [g], B. Ferrier [b,c], R. Ware [h], M. Pavolonis [i], T. Kuhn [j], J. Gurka [k], P. Liu [a], J. Cermak [l]

[a] Cloud Physics and Severe Weather Research Section, Environment Canada, Toronto, Ontario, Canada
[b] I.M. Systems Group, USA
[c] NOAA/NWS/NCEP, USA
[d] RPN, CMC, Environment Canada, Dorval, Quebec, Canada
[e] Meteorolooieches Institut, University of Bonn, Auf dem Hügel 20, 53121 Bonn, Germany
[f] Institute of Atmospheric Physics, Chinese Academy of Sciences, Beijing, China
[g] NCAR, Boulder, CO, USA
[h] Radiometrics Corporation, Boulder, CO, USA
[i] NOAA/NESDIS, Madison, WI, USA
[j] Lulea University of Technology, Division of Space Technology, P.O. Box 812, 981 28 Kiruna, Sweden
[k] NOAA/NESDIS, Greenbelt, MD, USA
[l] Ruhr-Universität Bochum, Department of Geography, 44780 Bochum, Germany

ARTICLE INFO

Article history:
Received 18 December 2013
Received in revised form 15 April 2014
Accepted 21 April 2014
Available online 13 May 2014

Keywords:
Ice fog
Arctic weather systems
Aviation
Visibility
Ice fog forecasting

ABSTRACT

The rate of weather-related aviation accident occurrence in the northern latitudes is likely 25 times higher than the national rate of Canada. If only cases where reduced visibility was a factor are considered, the average rate of occurrence in the north is about 31 times higher than the Canadian national rate. Ice fog occurs about 25% of the time in the northern latitudes and is an important contributor to low visibility. This suggests that a better understanding of ice fog prediction and detection is required over the northern latitudes. The objectives of this review are the following: 1) to summarize the current knowledge of ice fog microphysics, as inferred from observations and numerical weather prediction (NWP) models, and 2) to describe the remaining challenges associated with measuring ice fog properties, remote sensing microphysical retrievals, and simulating/predicting ice fog within numerical models. Overall, future challenges related to ice fog microphysics and visibility are summarized and current knowledge is emphasized.

Contents

* Corresponding author at: Environment Canada, Cloud Physics and Severe Weather Research Section, Toronto, Ontario, Canada. Tel.: +1 416 739 4607.
E-mail address: Ismail.gultepe@ec.gc.ca (I. Gultepe).

http://dx.doi.org/10.1016/j.atmosres.2014.04.014
0169-8095/

1. Introduction

Ice fog, which most often occurs in the high latitudes or high elevations at low temperatures, is an important but not well-understood phenomenon. Ice fog, often termed *pogonip* (derived from the Shoshone Native Americans word "payinappih") generally forms at temperatures (T) less than −15 °C and consists solely of ice crystals. The meteorological community, according to the American Meteorology Society (AMS) Glossary of Meteorology (Glickman, 2000), defines ice fog as an event consisting of single ice crystals that occur at T usually less than −30 °C. Ice nucleation activations at temperatures (<−10 °C) by deposition nucleation were stated by Young (1974). Gultepe et al. (2014) suggested that an ice fog particle forms usually due to deposition nucleation process over the saturated environments based on relative humidity with respect to ice (RH_i). Ice fog significantly reduces visibility (Vis) and can cause ice to accumulate on surfaces such as aircraft, power lines, and roads. As such, ice fog is a significant hazard. Unfortunately ice fog forecasting using operational numerical weather prediction (NWP) model is often very difficult (Gultepe et al., 2009, 2014) because of limited surface in-situ, ground based remote sensing, satellite observations, and limitations in understanding of the ice microphysics and nucleation process.

Reduced visibility and other weather events commonly play a major role in aviation related accidents over the Arctic regions. The Transport Canada Civil Aviation Daily Occurrence Reporting System (CADORS) available at www.tc.gc.ca reports that weather-related financial losses and deaths per capita in northern latitudes can be 30 times more than those of mid-latitudes. Considering the fact that Arctic waters will be more accessible in the near future, these numbers may reach much higher values. Records of aircraft accident fatalities in Canada during the period of Jan 1993 to June 2010 from CADORS indicate that

- in cases of aircraft accident fatalities, a weather event was cited as a contributing factor in 27% of accident cases (365/1351), with reduced visibility being cited in 14% of cases (192/1351).
- flying in the Canadian northern latitudes is more hazardous than in the rest of Canada, and weather is a major factor in the increased risk, particularly reduced visibility. The per capita rate of aviation related fatalities in the north is 18 times higher than the national rate.

When only cases where weather was a factor are considered, the aviation accident rate in the northern regions is 25 times higher than the national rate. If only cases, where reduced visibility was a factor, are considered, the average rate of occurrence in the north is about 31 times higher than the national rate. Ice fog occurrence is found about 20–25% of the time during the cold seasons (Gultepe et al., 2007a, 2007b, 2014). The earlier work suggested that cold fog most frequently occurred when the temperature was less than −30 °C. The later one showed that over 67 day ice fog was observed about 25% of time. Gotaas and Benson (1965) also showed that ice fog lasted 6 to 9 consecutive days (~25% of time over two months) during the winter of 1961–1962. Gultepe et al. (2007a) provided a figure showing occurrence of cold fog where cold fog forms at least 20% of times in the northern latitudes. These studies suggest that better understanding of ice fog prediction and detection is required over northern latitudes.

The goals of this review are: 1) to summarize the current knowledge of ice fog microphysics, as inferred from observations and NWP models, and 2) to describe the remaining challenges associated with measuring ice fog properties, remote sensing microphysical retrievals, and simulating/predicting ice fog within numerical models.

2. Earlier studies on ice fog

Earlier studies of ice fog conditions can be found in Thuman and Robinson (1954), Robinson et al. (1957), Benson (1965), Benson and Rogers (1965), and Ohtake (1967). Wendler (1969) described the ice fog as a dense cirrostratus cloud near the surface. Gotaas and Benson (1965) studied two extreme ice fog events and suggested that cooling near the surface is not completely attributed to cold air advection or heat losses from the air and snow surface. In their work, air T was less than −40 °C for two ice fog cases during the winter of 1961–1962. They proposed that heat flow to the ice

crystals was radiated away, creating strong T gradient close to the ice crystals. For these events, the air in contact with crystals had lower T and was saturated with respect to ice. In their work, ice fog is primarily defined as a man-made phenomenon.

Wexler (1936, 1941) and Gultepe et al. (2014) explained the existence of strong radiative cooling previous to an ice fog event, being limited by the higher T above the inversion layer (Fig. 1). Radiative cooling starts at low levels and spreads upwards, during which a strong surface inversion forms but decreases in strength with time. In particular, the sun can contribute more heat, resulting in warming. At higher levels, soon an isothermal layer forms and its thickness increases with time. The inversion top decreases with subsidence, resulting in a weak upper inversion. In another study, Bowling et al. (1968) suggested that ice fog events might also occur in Alaska due to advection of a cold dome from Siberia, resulting in an anti-cyclonic circulation. Then, subsidence warms the initial cold air above the surface layer, trapping the surface cold air where ice fog forms. These studies suggest that ice fog can be related to regional and larger scale processes.

Aircraft produced ice particles (APIPs) in supercooled cloud conditions can be seen over the airports or behind aircraft (Heymsfield et al., 2011; Woodley et al., 1991; Langmuir et al., 1948; Ludlam, 1956). Heymsfield et al. (2011) stated that the holes associated with inadvertent seeding of clouds with ice particles generated by aircraft, were produced through spontaneous freezing of cloud droplets in air that is cooled as it flows around aircraft propeller tips or jet aircraft wings. They concluded that polar clouds are particularly susceptible to the APIPs' effects because of modifications in the radiative processes. This may also suggest that sampled ice crystals by aircraft sensors over the Arctic environment may include APIPs and these conditions were also observed during Fog Remote Sensing And Modeling-Ice Fog (FRAM-IF) project (Gultepe et al., 2014).

The size of ice fog particles is usually less than 200 μm in length and their fall speed is similar to 10 μm droplets in case of warm fog/freezing fog particles (Koeing, 1970). Assuming that ice crystals form directly from vapor depositing onto IN (ice nuclei), their growth can be different than those of large ice crystals. Koeing (1970) proposed a method to calculate ice crystal growth rates by vapor deposition. If the supercooled droplets do not play a role in ice fog formation, vapor deposition directly onto IN is the major source for ice fog particle formation and growth. He stated that diffusional growth of small ice crystals was much larger than ventilation effects, suggesting that ice fog particles grew because of vapor

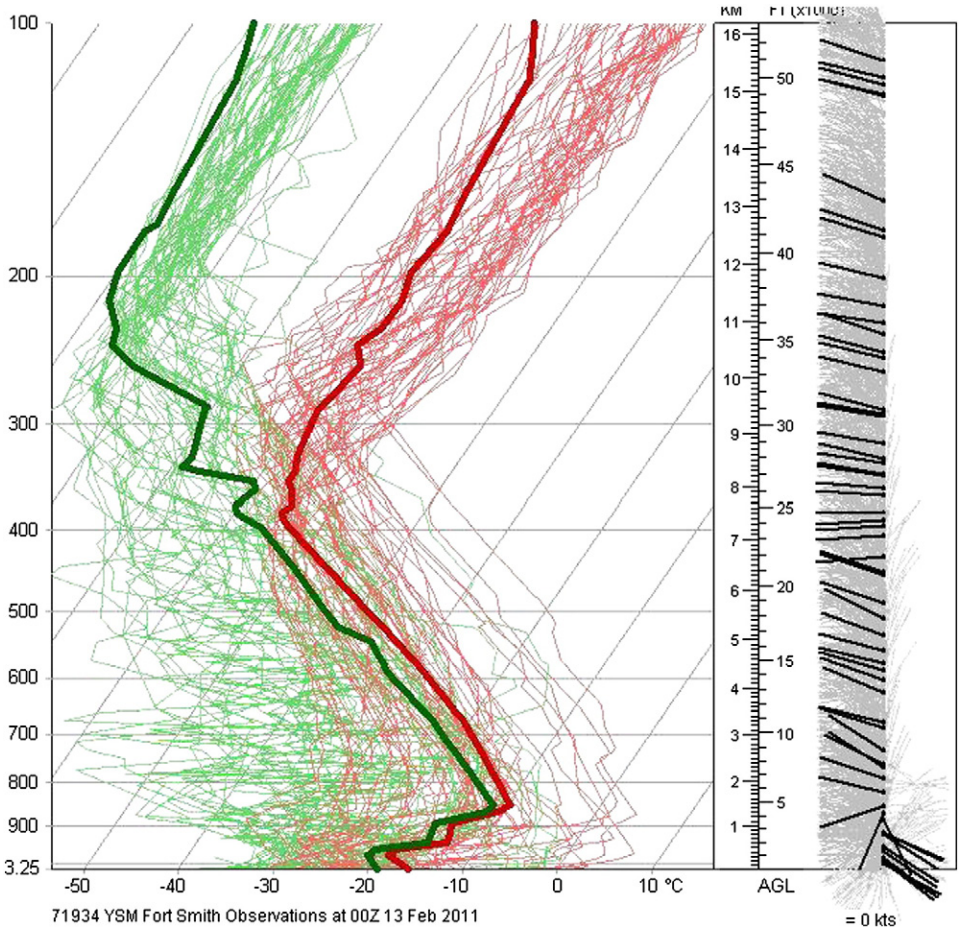

Fig. 1. A typical cold region boundary layer profile: T (red) and T_d (green) profiles from radiosonde measurements for entire January of 2011 (top); thick lines are for January 13, 2011 on 0000 UTC.

diffusion and was a strong function of crystal particle shape. Although IN composition and concentration play an important role for ice initiation (Zelenyuk et al., 2005), the IN concentration cannot be predicted or measured accurately (Gultepe and Isaac, 2002; Gultepe et al., 2014). Szyrmer and Zawadzki (1997) stated that ice forming nucleus issues remain an area of debate and the great majority of IN constitutes of soil mineral particles.

Many airborne sensors cannot measure accurately the ice particles with sizes less than 200 μm because of issues of shattering on the sensor tips and sensor optical sensitivity in the high speed environments (Gultepe et al., 2001; Lawson, 2011; Lawson et al., 2006a, 2006b; Field et al., 2006). Lately, the new sensors, e.g. in-situ 2-dimensional stereographic (2DS) optical probe (Lawson et al., 2010), were being used for small ice crystal detections both in the flight conditions and at the surface (Lawson et al., 2010, 2011). Lawson et al. (2006c) and Baker and Lawson (2006) made a detailed study of ice crystals using various in-situ instruments including a cloud imaging probe (CPI) and polar nephelometer (PN) at the South Pole Station; N_i was found up to 500 L^{-1} for sizes <200 μm and the largest N_i was usually at about 50 μm in max dimension, suggesting that small ice crystals were more abundant in high numbers. They also stated that these high numbers can be related to collection efficiency of the sensors, wind effects, and aspirator issues but their results did not encompass the full range of ice fog conditions. Referring to the work of Kumai (1964), Hobbs (1965) concluded that majority of ice crystal particles were spherical and 74% of ice particles collected consisted of aggregates of two or more spherical particles at T <−37 °C. A similar work by Korolev and Isaac (2003) also stated that, using SPEC Inc. CPI observations, ice crystals with sizes less than about 100 μm were spherical. These studies emphasized that the shapes of ice fog particles were mostly spherical for sizes less than 100 μm. In contrast, Gultepe et al. (2014) and Kim et al. (2014) suggested that this may not be the case because ice crystal shapes were not spherical but mostly pristine crystals in ice fog conditions.

The latest studies on cold fog (Velde et al., 2010; Gultepe et al., 2007a, 2007b) stated that accurate fog prediction critically depends on model horizontal and vertical resolutions, initial conditions, microphysical parameterizations, PBL turbulence, radiation, land–surface interactions, and air quality (Bergot et al., 2007; Bergot and Guedalia, 1994). Detailed studies of ice fog by Girard and Blanchet (2001), using a Northern Aerosol Regional Climate Model suggested that ice fog can significantly affect the radiative budget in the Arctic, and pointed out that ice fog may occur up to 30%–40% of the time in Arctic winter (Curry et al., 1990) and their radiative effect can be as high as 60 W m^{-2}.

The latest field and modeling studies of ice fog microphysical properties were provided by Gultepe et al. (2014) and Kim et al. (2014). These studies focused on ice fog that was related to depositional nucleation (over Yellowknife, NWT, Canada) and homogeneous nucleation (over Fairbanks, Alaska, USA) processes, respectively. Both studies provided detailed observations and numerical modeling of ice fog properties, and their studies are summarized below. These studies agreed that better instruments and observational techniques are needed to represent ice fog conditions in the numerical forecast and research models.

Based on the above studies, ice fog microphysical characteristics need to be better understood and a physically-based representation needs to be developed for numerical forecast model applications because the Arctic environment is very sensitive to small changes in moisture and temperature, leading to ice fog. A study by Gultepe et al. (2012) showed that accidents related to weather and low visibility over the northern latitudes will increase tenfold. This suggests that ice fog conditions can have major impacts on aviation and ground/water-based transportation, as well as on climate change at low temperatures where its impacts will be largest.

3. Instruments and measurements

Ice crystal measurements are usually done with aircraft based sensors at the surface (Gultepe et al., 2014; Lawson et al., 2006c). During FRAM projects, Gultepe et al. (2014) used various sensors representing ice crystal spectrum characteristics and meteorological parameters. Figures 2a and 2b show the instruments deployed at the Barrow, Alaska, Department of Energy (DOE) site and Yellowknife, NWT, Canada, respectively. The sensor list is given in Table 1. These instruments were selected to obtain visibility, snow rate and accumulated amount, solar and infrared broadband fluxes, 3D wind components at 1 Hz and 16 Hz sampling rates, snow reflectivity, vertical profile of T, vapor mixing ratio (Qv), and liquid water content (LWC). The Vaisala FD12p, Sentry, and Metek HSS SWS-200 Vis sensors were used to estimate uncertainty in ice fog Vis measurements.

Ice crystal particle and aerosol spectra and/or shape in Gultepe et al. (2014) were measured by optical sensors such as the Climatronic Aerosol Profiler (CAP, MetOne Inc.), the Ultra High Sensitivity Aerosol Spectrometer (UHSAS), a fog measuring device (FMD) (Fig. 3a), a ground cloud imaging probe (GCIP, Fig. 3b), a laser precipitation monitor (LPM), and OTT ParSiVel distrometer. The images of ice crystals were taken by a microscope (Fig. 3c) and an ice crystal imager (ICI, Gultepe et al., 2014). The GCIP sensor (Fig. 3b) adapted from an aircraft instrument called the DMT CIP probe has been developed for ground based measurements of ice fog and light precipitation. The small ice crystal size distributions of fog and snow particles over 62 channels were obtained at 1 s intervals. The resolution of the spectra is 15 μm, and min and max sizes are about 7.5 and 930 μm, respectively. The smallest image obtained represents particles less than about 10 μm.

Another detailed field project on ice fog was done by Kim et al. (2014). In their work, they used a Video Ice Particle Sampler (VIPS) probe to obtain ice crystal spectra and shape for particle sizes less than a few hundred microns. The VIPS is an electro-optical instrument used to collect and record a continuous sample of cloud particles down to 5 μm. The resulting imagery is available for real-time, in-flight evaluation of cloud conditions and for post-flight habit classification and size distribution analysis. The instrument is calibrated with test beads and it is accurate to a 1–2 μm in diameter (Kim et al., 2014). Their results were similar to Gultepe et al. (2014) but the measurements were mostly related to homogeneous nucleation processes.

4. Ice fog parameterizations

Ice fog parameterizations have only recently been developed because of limited measurements at cold temperatures

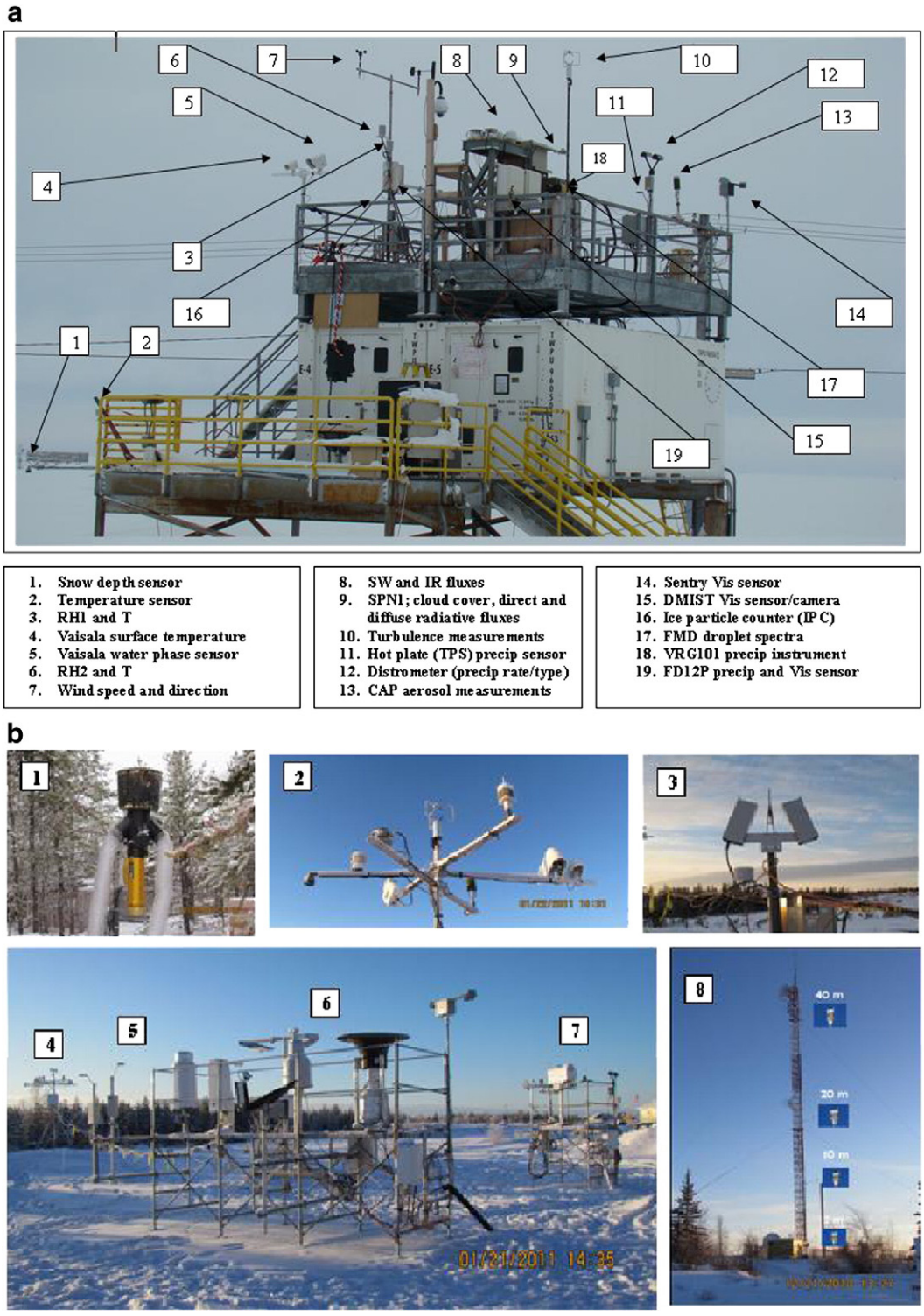

Fig. 2. Instruments used during FRAM-IF projects took place over Barrow, Alaska, US DOE, North Slope Alaska (NSA) site (a) and over Yellowknife, NWT, Canada (b) where numbers represent the locations of sensors given in Table 1.

and instrumental limits. Likewise, ice fog parameterizations are not generally utilized in numerical weather prediction models (NWPs). Ice fog can form mainly with two types of nucleation: 1) heterogeneous nucleation (deposition nucleation, Gultepe et al., 2014) and 2) homogeneous nucleation (Kim et al., 2014). In the Arctic boundary layer, a strong inversion usually exists and its top can be about −5 to −10 °C where, because of radiative processes, smaller droplets may form, resulting in ice fog

Table 1
Instruments deployed during the FRAM-IF fog project that took place over Yellowknife International Airport, North West Territories, Canada. The (Location) given in first column is for the instrument location at the project site (see Fig. 2). Tr represents the trailer location. RH_w is the relative humidity with respect to water and T is the temperature.

(Location) instruments	Definition	Measurement	Characteristics
(7) FMD (Droplet measurements Technologies Inc.)	Fog monitoring device	Droplet spectra	1–50 μm size range
(1) GCIP (Droplet Measurements Technologies Inc.)	Ground imaging probe	Droplet/ice spectra	15–930 μm size range
(7) OTT ParSiVel (Metek Inc.)	Parsivel size velocity distrometer	Precipitation spectra	400 μm-max size range
(2) CAP (Climatronics Inc.)	Climatronics aerosol profiler	Droplet and aerosol spectra	0.3–10 μm; 8 channels
(6) T-200B (GEONOR Inc.)	Precipitation sensor	Precipitation amount	Lower threshold 0.5 mm h^{-1}
(4) IPC (York University)	Ice particle counter	Ice particle spectra	15–500 μm
(6) FD12P (Vaisala Inc.)	All weather precipitation sensor	Precipitation type and amount, and visibility	0.05 mm h^{-1}; lower threshold
(6) Sentry visibility (Envirotech Inc.)	Sentry visibility sensor	Visibility	>10 m lower threshold
(5) CL31 (Vaisala Inc.)	Ceilometer	Ceiling height	>10 m uncertainty
(2) TPS (Yankee Environmental Systems Inc.)	Total precipitation sensor	Total precipitation rate and amount	>0.25 mm h^{-1} lower threshold
(2) DSC111 (Vaisala Inc.)	Surface state condition sensor	Surface type and condition	–
(2) DST111 (Vaisala Inc.)	Surface state temperature sensor	Surface temperature	–
(2) SR50 (Campbell Scientific Inc.)	Sonic ranger for snow depth	Snow depth	10–20% uncertainty
(4) SW/IR radiometers (Eppley Inc.)	Shortwave/infrared radiometers	SW and IR broadband fluxes	10–15% uncertainty
(2) UW 3D sensor (Young Inc.)	Ultra wind 3-dimensional sensor	3D wind speed and direction, turbulence	4–32 Hz sampling rate
(4) Young wind sensor (Young Inc.)	2-dimensional wind sensor	2D wind speed and direction	1 min sampling rate
(2) SPN1 (AT Delta Inc.)	Sunshine pyronometer	Direct; diffuse SW radiation	0.4–2.7 μm
(6) MRR (Biral Inc.)	MicroWave rain radar	Precipitation reflectivity and Doppler velocity	–
(7) MP-3000 MWR (Radiometrics Corp.)	Profiling microwave radiometer	LWC, temperature, humidity, and RH_w profile	Liquid water content threshold >0.1 g m^{-3}
(Tr) Microscope (Barska)	–	Ice crystal pictures	–
(2) RID 872E3 (Campbell Scientific Inc.)	Rosemount icing detector	Icing rate	Liquid detection: 10%
(Tr) UHSAS (Droplet Measurements Technologies Inc.)	Ultra High Sens. aerosol spectrometer	Aerosol spectra	0.050–1 μm size range
(2) Pressure sensor (Vaisala Inc.)	–	Pressure	1% uncertainty
(2) WXT520 (Vaisala Inc.)	Present weather sensor	T, RH_w, wind speed and Direction, rain, pressure	10% uncertainty
(4) CNR1 (Kipp&Zonen Inc.)	Net radiometer	SW and IR up and down radiative fluxes	Pyronometer: 0.305–2.8 μm Pyrgeometer: 4.5–42 μm
(6) SWS-200 (Biral Inc.)	Present weather sensor	Precipitation and visibility	10% uncertainty
(7) LPM 5.4110 (Biral Inc.)	Laser precipitation monitor	Precipitation spectra	0.13–8 mm; 22 channels
(4) HMP45 (Campbell Scientific Inc.)	Temperature and humidity probe	T and RH_w	Uncertainty: 1 °C for T and 10% for RH_w
(4) HMP45C212 (Campbell Scientific Inc.)	Temperature and humidity probe	T and RH_w	Uncertainty: 1 °C for T and 10% for RH_w
(7) MP100A (Rotronic Inc.)	Temperature and humidity probe	T and RH_w	Uncertainty: 1 °C for T and 10% for RH_w
(Tr) ICI (Lulea Technical University)	Ice crystal imager	Ice crystal spectra	>100 detection threshold
(7) IceMeister-9734 (New Avionics Inc.)	Icing sensor	Icing condition	5% uncertainty
(Tr) IR (DX501)/IRtC.20A-oE (Exergen Inc.)	Infrared temperature sensor	Ceiling temperature	5% uncertainty
(3) POSS (Environment Canada)	Precip. Occur. sensing system	Precipitation type and spectra	>500 μm for detection limit
(Tr) Axis camera system (AXIS Comm. Inc.)	IP camera system	Pictures	–

formation. However, dissipation of these fog conditions may occur by falling particles. It is important to note that both nucleation processes should be included in the numerical forecasting of ice fog at cold temperatures.

In the following subsections, ice fog prediction issues will be discussed and the current state of ice fog microphysical parameterizations will be summarized.

4.1. Ice fog coverage using RH_i

Ice fog forecasting is usually not performed with forecasting models because ice water content (IWC) and ice crystal number concentration (N_i) are usually not accurately obtained from existing microphysical algorithms (Gultepe et al., 2001, 2014). Ice fog occurs when RH_i is approximately greater than 100%. Ice fog may occur because of deposition nucleation processes that depend on ice nucleus size, concentration, available moisture, and T. Gultepe et al. (2003) found that frost point temperature (T_f) can be related to dew point temperature (T_d) as:

$$T_f = T_d + \Delta f, \quad (1)$$

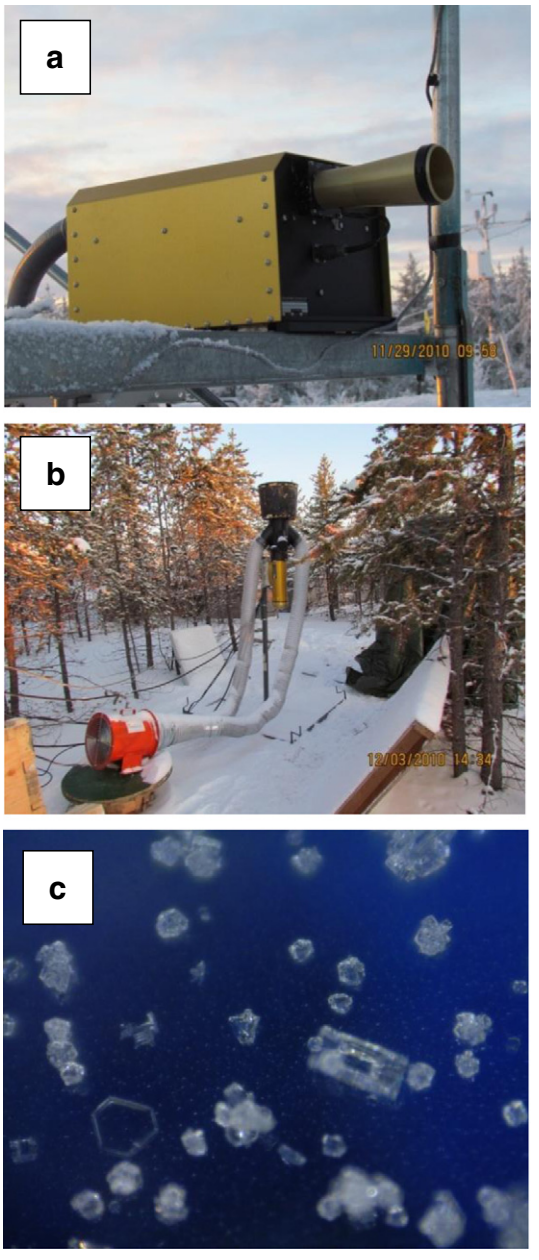

Fig. 3. Droplet Measurement Technologies (DMT) fog measuring device (FMD) (a), DMT Ground cloud imaging probe (GCIP) (b), and ice fog particles collected during FRAM-IF project over Yellowknife International Airport on January 18, 2011 (c).

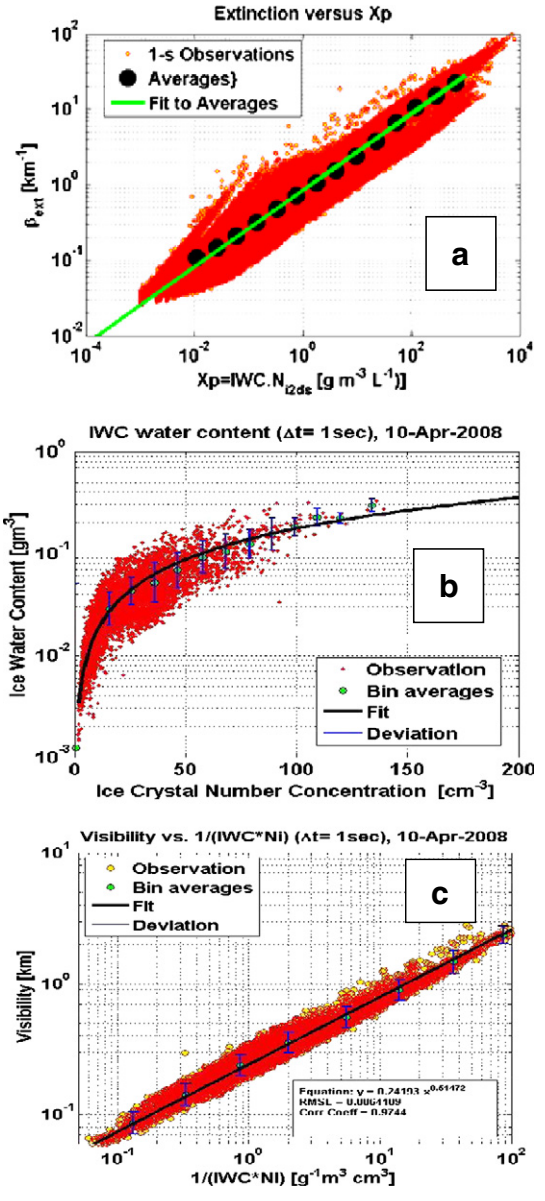

Fig. 4. Scatter plot of extinction coefficient (β_{ext}) versus the product of IWC and N_{i2ds} for the entire dataset. The green line is for the best fit to the mean values shown with filled black circles from aircraft based 2DS probe ice crystal measurements collected during FRAM-IF project in DOE NSA site (a), IWC versus N_i from FMD probe (b), and Vis versus (IWCxN_i) (c). The solid lines are fits and bars represent sd.

where T_d [°C] and T_f [°C] were obtained using LiCOR instrument humidity measurements (Gultepe et al., 2003) and their difference is parameterized as

$$\Delta f = p_1 T_d^3 + p_2 T_d^2 + p_3 T_d^1 + p_4, \tag{2}$$

where $p_1 = 0.000006$; $p_2 = -0.0003$; $p_3 = -0.1122$; and $p_4 = 0.1802$. If T_d is known, then T_f [°C] is calculated using Eqs. (1) and (2). The following equation is given for saturated vapor pressure by Murray (1967) as

$$e_s = 6.1078 \exp\left[\frac{a(T-273.16)}{(T-b)}\right], \tag{3}$$

where T [K], e [mb], a = 21.8745584 (17.2693882); b = 7.66 (35.86) over the ice (water) surface. Then, using T_f and T, RH_i is obtained from the following equation

$$RH_i = \frac{e_i(T_d + \Delta f)}{e_{si}(T)}. \tag{4}$$

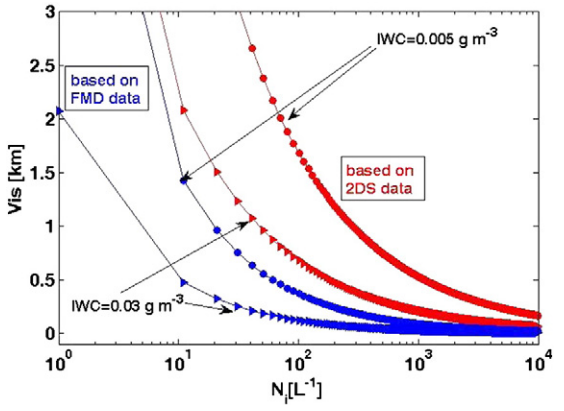

Fig. 5. Visibility obtained from the two techniques using Eq. (5) (red lines represent 2DS probe data) and Eq. (6) (blue lines represent FMD data). The triangles are for IWC = 0.03 g m^{-3}, and the circles are for IWC = 0.005 g m^{-3}. Note that for smaller N_i values (say 10 L^{-1}), Vis ranges from 0.5 km up to ~5 km for different sensors.

If RH_w and T are known, then T_d is calculated using an equation similar to Eq. (12) but for water. Using Eqs. (1)–(4), RH_i is then calculated. If RH_i is approximately ~100% and T <— 10 °C, then ice fog regions can be obtained from model simulations.

4.2. Visibility for ice fog

Ice fog can be parameterized assuming that Vis is a function of both IWC and N_i at sizes usually less than 200 μm. In this size range, particle terminal velocity (V_t) can be about 1 cm s^{-1} depending on its shape and size. This suggests that ice fog crystals can fall through the air about 36 m over 1 h time period. However, if their V_t is about 1 mm s^{-1}, then they fall only about 4 m. This shows that for any model to correctly predict ice fog visibility should be sensitive to low IWC (0.001 g m^{-3}), V_t, and high N_i values (>1000 L^{-1}) (Gultepe et al., 2008, 2014). Based on in-situ measurements, the next section provides parameterizations for ice fog visibility versus both IWC and N_i.

4.3. Gultepe et al. parameterization for ice fog visibility

Gultepe et al. (2014), using low level flying aircraft observations and surface in-situ observations (collected during FRAM-IF project), representing depositional nucleation conditions, obtained a parameterization of extinction coefficient (β_{ext} or Vis) as a function of N_i and IWC (Fig. 4a). If the cross-section surface area (A_c) is related to a crystal mass e.g. $m_i = aA_c^b$ (Lawson, 2011), then $\beta_{ext,}$ using 2DS optical probe Vis from low level Arctic clouds collected over the FRAM project site (Gultepe et al., 2014) can be written as a function of IWC and total N_i (similar to Gultepe et al., 2007a, 2007b). Then, using a relationship between Vis and β_{ext}, Vis parameterization for ice crystals between 10 and 500 μm can be considered as

$$Vis_1 = 1.19(IWC \cdot N_i)^{-0.5066}. \quad (5)$$

Using FMD (from DMT Inc.) measurements with sizes less than 50 μm collected during FRAM-IF project in Barrow, Alaska, on April 10, 2008, another parameterization (Fig. 4b, c) is also given by

$$Vis_2 = 0.24(IWC \cdot N_i)^{-0.5147}. \quad (6)$$

If IWC and N_i are known from a forecasting model at the each time step, then Vis (or β_{ext}) can be obtained from Eqs. (5) or (6). Gultepe et al. (2014) using FMD probe measurements calculated N_i for deposition nucleation events as much as 1000 L^{-1} or more (Fig. 4b).

Assuming N_i from 1 to 10^4 L^{-1} while IWC changes from 0.005 to 0.03 g m^{-3}, Fig. 5 is obtained using the results of both Eqs. (5) and (6). This figure suggests that based on FMD and 2DS measurements, Vis can be significantly different, representing instrumental limitations on the measurements. Note that Eq. (5) represents relatively large particles compared to Eq. (6) which shows much higher contributions from small particles (50 μm). When N_i >1000 L^{-1}, both equations result in similar values of Vis of about 100 m. This result should be considered cautiously because of limited measurements done over ice fog conditions. Also, increasing IWC reduces visibility obtained from Eq. (6) more than this of Eq. (5).

The N_i is usually obtained from the equation given for deposition–freezing nucleation (Meyers et al., 1992) as

$$N_{id} = \exp(a + b[100(S_i - 1)]. \quad (7)$$

In Eq. (7), a = −0.639 and b = 0.1296, and S_i is the super saturation with respect to ice. The maximum N_i values from Eq. (7) can reach up to 100 L^{-1} at T = −20 °C that is much less than observed ice fog N_i values observed during Fog Remote Sensing and Modeling-Ice Fog (FRAM-IF) project which took place over Yellowknife International Airport during winter of 2010–2011. Therefore, for WRF simulations discussed later, we subjectively increased N_i 10 times to represent observed N_i values that may not be true always, but better represent the N_i for ice fog conditions.

4.4. Ohtake and Huffman parameterization for ice fog visibility

If IWC is prognostically obtained, then Vis for ice fog, assuming that N_i and mean equivalent mass diameter (d) are known, can be obtained (Ohtake and Huffman, 1969) as

$$Vis = \frac{1}{3}\left[3.2\frac{IWC}{N_i}\right]^{1/3} - 1.5\bar{d}. \quad (8)$$

Eq. (8) shows how ice fog Vis changes with IWC, N_i, and d (mean diameter). This equation was developed over Fairbanks, Alaska, representing likely homogeneous nucleation processes. In their work, N_i and d were assumed as 200 cm^{-3} and 7.2 μm (for high IWC e.g. > 0.1 g m^{-3}), and as 80 cm^{-3} and 4.5 μm (for low IWC e.g. > 0.01 g m^{-3}). If ice crystals form due to deposition of vapor directly onto ice nuclei at cold T, N_i can be parameterized as a function of RH_i. A relationship between N_i and RH_i for ice fog does not currently exist.

4.5. N_i estimation by homogeneous nucleation

Ice crystal number concentration calculations based on the classical theory of homogeneous nucleation suggests that its value is usually less than observed values and unreliable; and therefore, its parameterization is generally used for N_i prediction that over the ocean it can reach up to 10^4 particles per cm^{-3} with sizes less than 0.1 μm (haze particles). Homogenous nucleation rate based on sulfuric acid-water particles can be estimated using an equation given by Jaecker-Voirol and Mirabel (1989) as

$$J_{hom;h} = 10^x, \tag{9}$$

where

$$x = 7.0 - (64.24 + 4.7RH_f) + (6.13 + 1.95RH_f)\log_{10}N_{H_2SO_4}. \tag{10}$$

J_{hom} is the new production of sulfuric acid-water particles (# cm^{-3} s^{-1}) and RH_f is the RH with respect to water in a fraction value. $N_{H_2SO_4}$ is the number concentration of gas-phase sulfuric acid molecules (molecules cm^{-3}). This equation does not depend on temperature directly but through RH fraction and it is valid between 230 K and 300 K. Koop et al. (2000) also provided homogeneous nucleation rate calculation equations as a function of water activity for haze particles and it was used by Kim et al. (2014). The later stated that high concentrations of ice fog particles were present when homogeneous nucleation events occurred.

A similar equation but for homogeneous freezing nucleation rate of the droplets as a function of temperature is given by DeMott et al (1994) as follows

$$J_{hom;f} = 10^y, \tag{11}$$

where

$$y = -606.3952 - (52.6611T) - \left(1.7439T^2\right) - \left(0.0265T^3\right) - \left(1.536 * 10^{-4}T^4\right). \tag{12}$$

The above equations for ice fog visibility prediction can be used for homogenous nucleation events associated with power generation units, Arctic leads or polynyas, or with a low level inversion layer near the surface. When the nucleation rate is known, the number of freezing droplets can be obtained using an equation given in DeMott et al. (1994) and Kim et al. (2014) as

$$N_{i;hom} = \sum_{i=1}^{k}((1 - \exp - J_{hom}V\Delta t)n(D)\Delta D), \tag{13}$$

where V is the droplet volume, t time, and n(D) droplet spectra. Then, Eq. (13) (using Eqs. (9) and (11)) can be used to obtain N_i. Using either Eq. (5) or Eq. (6) and knowing both N_i and IWC, ice fog Vis can then be predicted with a NWP model. Use of the above equations in the model simulations are discussed in Section 6.

5. Relationship between visibility and extinction

The visibility parameterization in the previous section is obtained using a relationship between Vis and β_{ext}. In the following subsections, day and night time applications of Vis parameterizations for integrated conditions, including RH_i, ice fog, and light snow, are given.

5.1. Visibility definitions

Meteorological Observation Range (MOR) definition by the World Meteorological Organization (WMO) is based on Koschmieder law. Assuming a brightness contrast threshold (ε) of 0.05, daytime visibility (Vis_d) is given as

$$Vis_{d5} = 2.996\beta_{ext}{}^{-1}, \tag{14}$$

where $\ln(1/\varepsilon) = 2.996$. β_{ext} is the extinction coefficient given as

$$\beta_{ext} = \sum_{i=1}^{m}\pi Q_{ext}(r)n(r)r^2dr, \tag{15}$$

where Q_{ext} is the extinction efficiency and equals ~2 for large particles and may be calculated from Mie theory. For ice crystals, it depends on particle shape, particle spectra, and visible light wavelength.

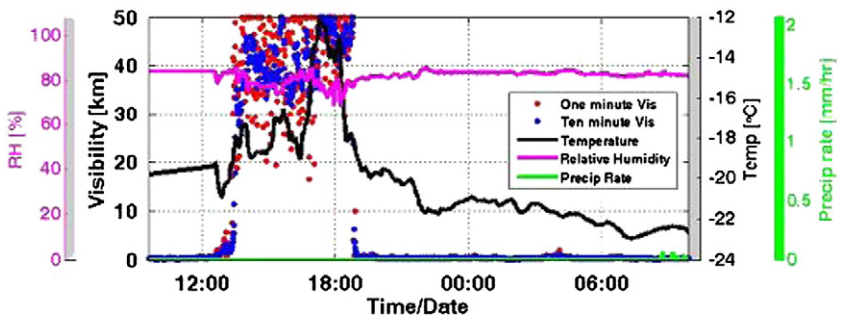

Fig. 6. Shows a time series of relative humidity with respect to water (RH_w), Vis, temperature (T), and precipitation rate (PR) on April 10, 2008 during FRAM-IF project at the DOE NSA site.

5.2. Relationship between day and night time visibilities

Using $\varepsilon = 0.02$ (threshold of luminance contrast or brightness contrast), Eq. (14) is also given as

$$Vis_{d2} = 3.912\beta_{ext}{}^{-1}, \quad (16)$$

where ε is defined as $(B_r - B_b) / B_b$, B_r is the apparent luminance of the object at range R and B_b is the apparent luminance of the background of the object at range R. In the Rapid Update Cycle (RUC) model (Benjamin et al., 2004) Vis is obtained by setting $\varepsilon = 0.02$ so that Vis_{d5} should be converted to Vis_{d2} as

$$Vis_{d2} = 1.3Vis_{d5}. \quad (17)$$

In general, measurements from Vis sensors (e.g. the FD12P, Fig. 6) are given based on the WMO MOR definitions. Fig. 6 shows time series of RH, Vis, precipitation rate, and temperature collected by FD12p and HMP45C212 sensors during a heavy ice fog event that occurred over Barrow, Alaska. It is interesting that the temperature increases during the ice fog formation from −20 °C to almost −18 °C at 1200 LST. Perhaps, this is due to latent heat release from nucleation plus deposition processes.

5.3. Nighttime definition of Vis

The nighttime Vis (Vis_n) definition is based on the simplified Allard's law as

$$Vis_n = \frac{I_o}{C_{DB}} \exp(-\beta_{ext} Vis_n), \quad (18)$$

where C_{DB} and I_o are usually about 0.084 miles^{-1} and 25 cd, respectively. Comparing Vis_d [km] versus Vis_n [km], using the assumed coefficients in Eq. (18), a simplified equation can be obtained as

$$Vis_n = 1.851Vis_d{}^{0.814}. \quad (19)$$

For forecasting applications, measurements done with instruments (if they do not perform processing internally) should be converted to nighttime visibilities using Eq. (19).

Equations given for ice fog Vis as function of (IWC,N_i), and for RH_i can be used to obtain integrated Vis values. In the case of both fog and precipitation occurring together, individual Vis values are first converted to extinction coefficients (β_{ext}) using Eq. (14), then, an integrated extinction coefficient is obtained as

$$\beta_{int} = \beta_{RHi} + \beta_{IWC_{IF}} + \beta_{IWC_{SN}}, \quad (20)$$

where the terms on right hand side of Eq. (20) represent extinction coefficients due to RH_i, and ice fog and snow water contents, respectively. The integrated Vis for ice fog while snowing is then calculated using β_{int} as follows:

$$Vis_{ice} = 3.912\beta_{int}{}^{-1}. \quad (21)$$

6. Numerical forecast models for ice fog prediction

In this section, numerical forecasting models that have been used for ice fog simulations were summarized.

6.1. GEM LAM model

Environment Canada (EC) currently runs the Global Environmental Multi-scale (GEM) (Côté et al., 1998) forecast model in a limited-area model (LAM) configuration over various domains in Canada with a 2.5-km horizontal grid spacing. In 2014, a pan-Canadian domain was added to this system which greatly increases the coverage over the Arctic. In this NWP system, most of the clouds and precipitation are predicted by the grid-scale condensation scheme, the 2-moment version of the Milbrandt and Yau (2005a,b) bulk microphysics parameterization (hereafter "MY2"). In this scheme, ice crystals are represented by two categories, "ice" representing pristine crystals and "snow" representing larger crystals (D > 250 μm) and/or aggregates, each of whose particle size distributions (PSDs) are represented by complete gamma functions whose parameters evolve along with the two prognostic variables (for each category x), the total number concentration, Nx, and the mass mixing ratio, qx. Currently, MY2 includes this process using the parameterization of Meyers et al. (1992). This parameterization, however, is based on limited aircraft and laboratory measurements that do not represent the Arctic conditions. Therefore, use of ice fog visibility parameterizations developed based on measurements of N_i and IWC in the current MY2 scheme may be problematic. However, the new measurements can be used to constrain the scheme for the prediction of N_i, and thus ultimately improve the prediction of visibility in ice fog in the model.

6.2. North American Mesoscale (NAM) model

For operational applications, NCEP's 12-km NAM model (Rogers et al., 2009; Ferrier et al., 2002) is used for regular weather guidance over continental US (i.e. the CONUS), Alaska, Hawaii and Puerto Rico. The NAM runs 4 times per day (00, 06, 12 and 18 UTC), providing forecast guidance over all of North America for hourly products out to 36 h, and also for 3-h products out to 84 h. The NAM post processor calculates visibility using a method that assumes the extinction is a function of cloud IWC (Stoelinga and Warner, 1999); however, this may result in more than 50% uncertainty in the ice fog Vis (Gultepe et al., 2009). Considering that the model has a high bias in RH and its IWC near the ground, two re-diagnosis methods for the ice fog conditions were performed. The first one uses surface parameters from the NAM (Zhou and Du, 2010) and predicts the occurrence of ice fog but not IWC. The second method uses a physically-based post-processing analysis from which IWC at height z can be diagnosed. Based on the mass balance equation for various physical processes given in Zhou and Ferrier (2008) and Zhou (2011), IWC is obtained as

$$IWC(z) = \left[\frac{(\beta \cdot C_o + adv) \cdot H_{sat}}{\alpha}\right]^{1/2} \left[\left(1 - \frac{z}{H_{sat}}\right)^{1/2} - \frac{2}{1 + e^{z/\delta}}\right], \quad (22)$$

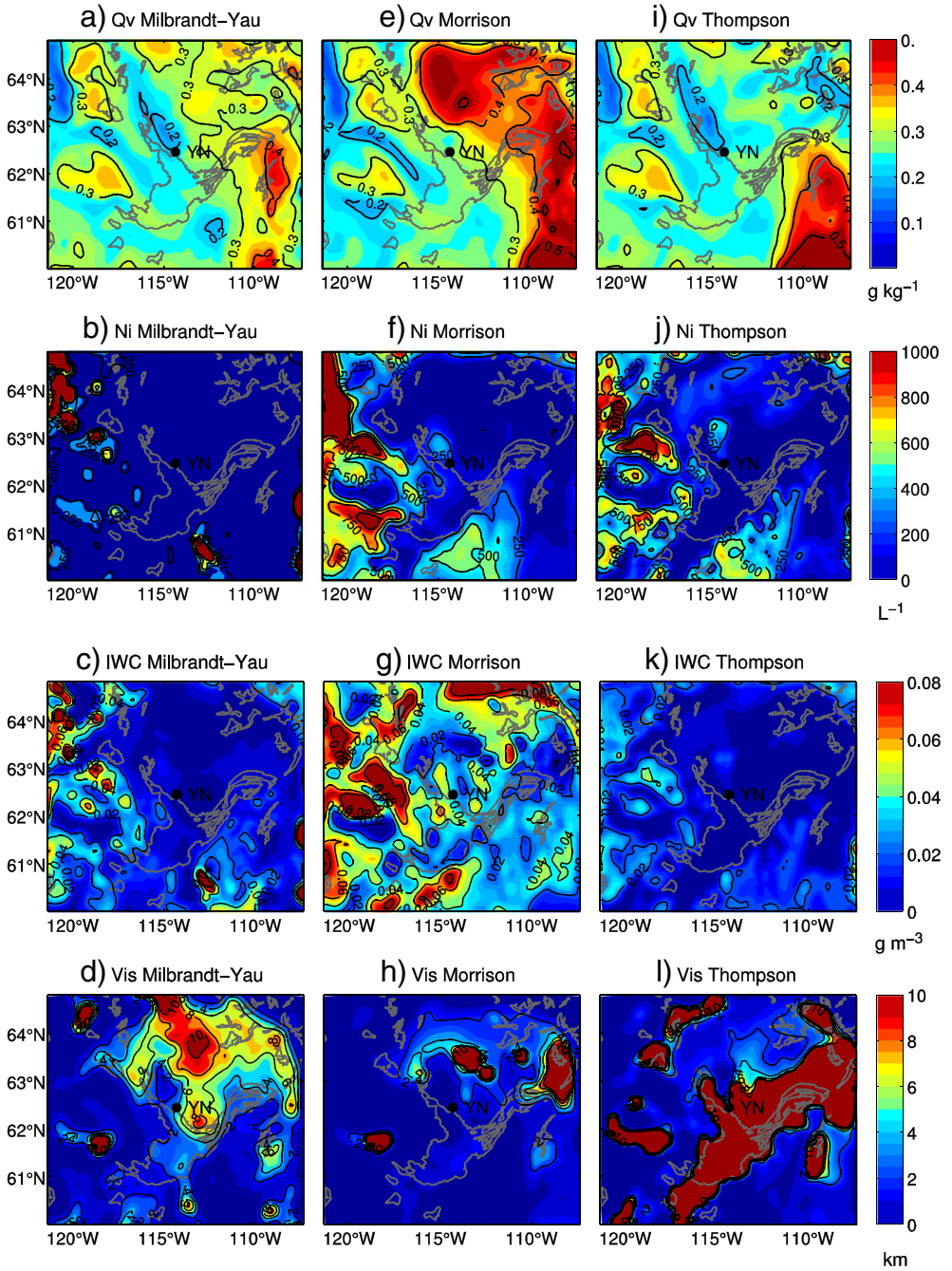

Fig. 7. The Q_v, N_i, IWC, and Vis obtained from the WRF simulations (using 10 km grid resolution) on 08:00 LST, January 12, 2011 over Yellowknife International Airport are shown in subpanels a–d for Milbrandt and Yau, in subpanels e–h for Morrison et al., and in subpanels i–l for Thompson et al. schemes, respectively.

where

$$\delta = \frac{K}{2[\alpha(adv + \beta \cdot C_o) \cdot H_{sat}]^{1/2}}, \tag{23}$$

and β is a function of both temperature and surface pressure, C_o the average cooling rate within the fog layer, *adv* the moisture advection, α the ice crystal gravitational settling parameter, K the turbulence exchange coefficient, H_{sat} the ice fog layer depth with $RH_i \geq 100\%$. During the FRAM-IF project, a test done using the second method significantly improved the prediction of the ice fog events. However, since ice fog within the boundary layer was not solely dependent on moisture advection, more research in this area is needed.

6.3. Simulations using WRF model

The WRF (Weather Research and Forecasting) model version 3.4.1 (Nygaard et al., 2011) was employed in the ice fog simulations. Two nested domains were used with a horizontal grid of 100 × 78 (30 km) and 88 × 64 (10 km resolution), respectively. The 35 vertical layers from the surface up to 100 hPa were utilized. Initial and boundary conditions were obtained using NARR (North American Regional Reanalysis) data. Simulations were conducted from 11 to 16 January of 2011. The WRF model (Nygaard et al., 2011) based on three microphysical algorithms is used for the simulations of Qv, fog IWC, N_i, and Vis. These microphysical algorithms are 1) Milbrandt and Yau scheme (Milbrandt and Yau, 2005a,b), 2) Morrison scheme (Morrison et al., 2005; Morrison and Milbrandt, 2011), and 3) Thompson scheme (Thompson et al., 2004, 2008).

The simulation results were compared to observations collected during FRAM-IF project (Gultepe et al., 2014) that took place in Yellowknife, NWT, Canada. Results suggested that none of the simulations provided accurate Qv, IWC, N_i, and Vis predictions. This was likely related to uncertainties in the individual ice microphysical scheme developed for clouds, but there might also be other reasons for this, such as the relatively coarse vertical resolution in the boundary layer. However, the simulations illustrate the potential for a mesoscale model to simulate ice fog, and the resulting reduction in visibility, and also the large sensitivity to the microphysics parameterization and the need to properly constrain the microphysics schemes with observations. It is clear that N_i prediction based on depositional ice nucleation mode underestimates N_i for ice fog conditions. In order to compensate for this, N_i values were increased 10 times to have comparable ice fog N_i values given in Gultepe et al. (2014). The results obtained on 08:00 LST on January 12, 2011 over Yellowknife International Airport from 10 km grid resolution are shown in Fig. 7a–d for Milbrandt and Yau scheme, Fig. 7e–h for Morrison scheme, and Fig. 7i–l for Thompson scheme, respectively. All three of these schemes have 2-moment treatment for the ice crystal category, predicting the ice mixing ratio and number concentration independently. However, they differ in their specific parameterizations of nucleation and growth processes.

The values of simulated Q_v, 10xN_i, IWC, and Vis (Fig. 7) are significantly different for all microphysical schemes but

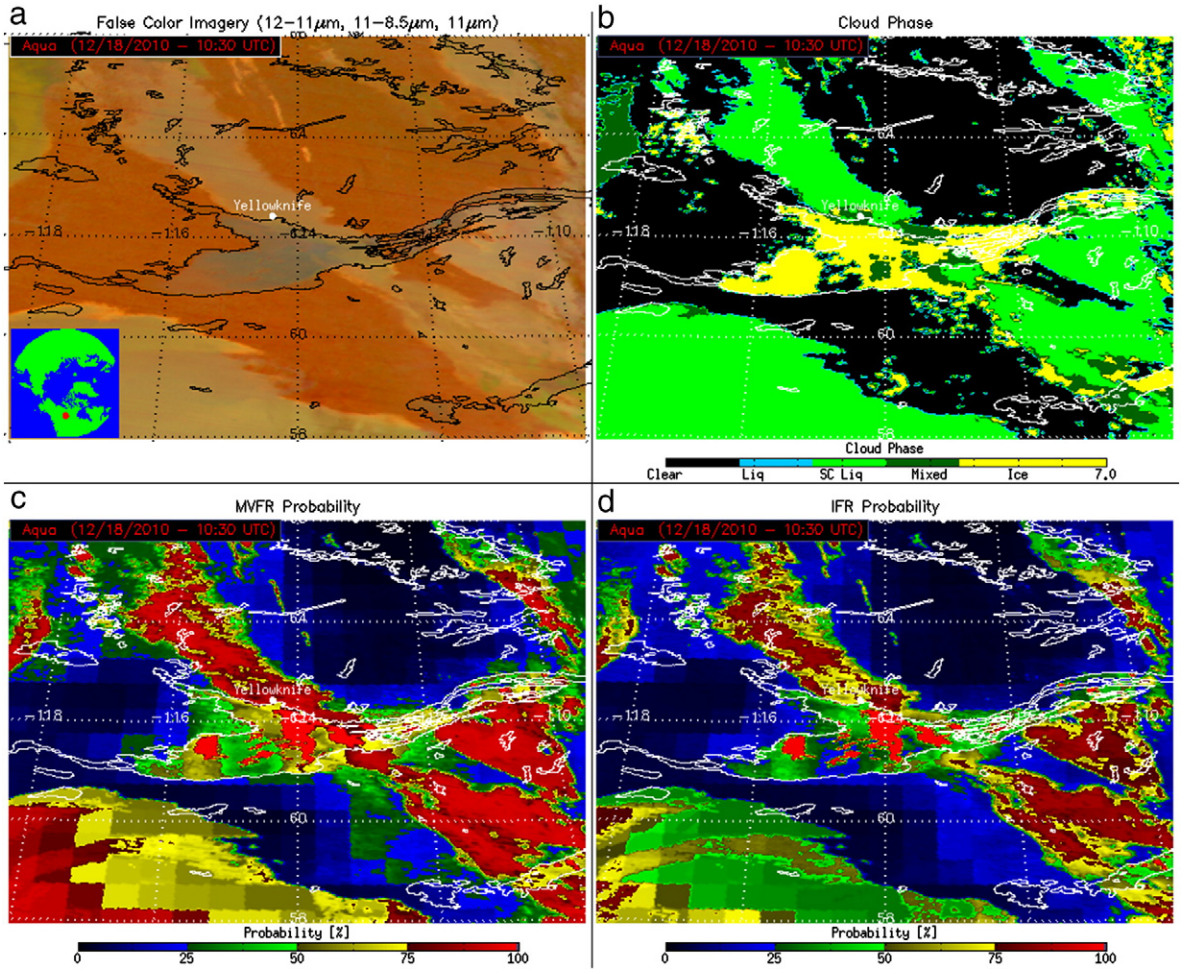

Fig. 8. An *Aqua* MODIS overpass at 10:30 UTC on December 18, 2010 is used to demonstrate cloud phase and low cloud base detection algorithms developed for GOES-R. A false color image is shown in (a). The GOES-R cloud phase product is shown in (b). The GOES-R probability of MVFR ceilings and probability of IFR ceilings are shown in (c) and (d), respectively.

comparable to observations. The reference simulations were performed using only N_i values but the results for Vis predictions were not comparable to observations. This suggests that we need to focus on better microphysical parameterization schemes for N_i and IWC for ice fog events. Otherwise, present ice fog microphysical schemes cannot be used for predictions of Vis.

6.4. Forecasting issues

As pointed out in the previous sections, ice fog can be parameterized assuming that Vis is a function of IWC (ice water content) and N_i (~1000 L^{-1}) at sizes usually less than 200 μm. In this size range, particle terminal velocity (V_t) can be about 1 cm s^{-1} depending on its shape and density. This shows that for any model to correctly predict ice fog visibility it should be sensitive to low IWC and high N_i values (Ohtake and Huffman, 1969; Gultepe et al., 2008, 2014). The current forecasting models were not designed for ice fog occurring over the Arctic regions. In fact, ice fog occurrence in various space and time scales in a 3D volume can complicate its accurate prediction (Mueller et al., 2010). The major issues for ice fog predictions are related to prediction of small ice crystals N_i and IWC, and limitations in the ice microphysical parameterizations in the cold temperatures. Clearly, deposition nuclei and radiative processes in the clear Arctic boundary layer conditions and existence of a weak or strong inversion need to be predicted accurately to obtain ice fog visibility and related ice microphysical parameters.

7. Remote sensing monitoring of ice fog

7.1. Satellite based monitoring

Earlier studies on fog detection using Geostationary Operational Environmental Satellite (GOES) and other geostationary observations can be found in Wetzel et al. (1996), Lee et al. (1997), Gultepe et al. (2007), and Cermak and Bendix (2008). Passive low earth orbit and geostationary satellite measurements

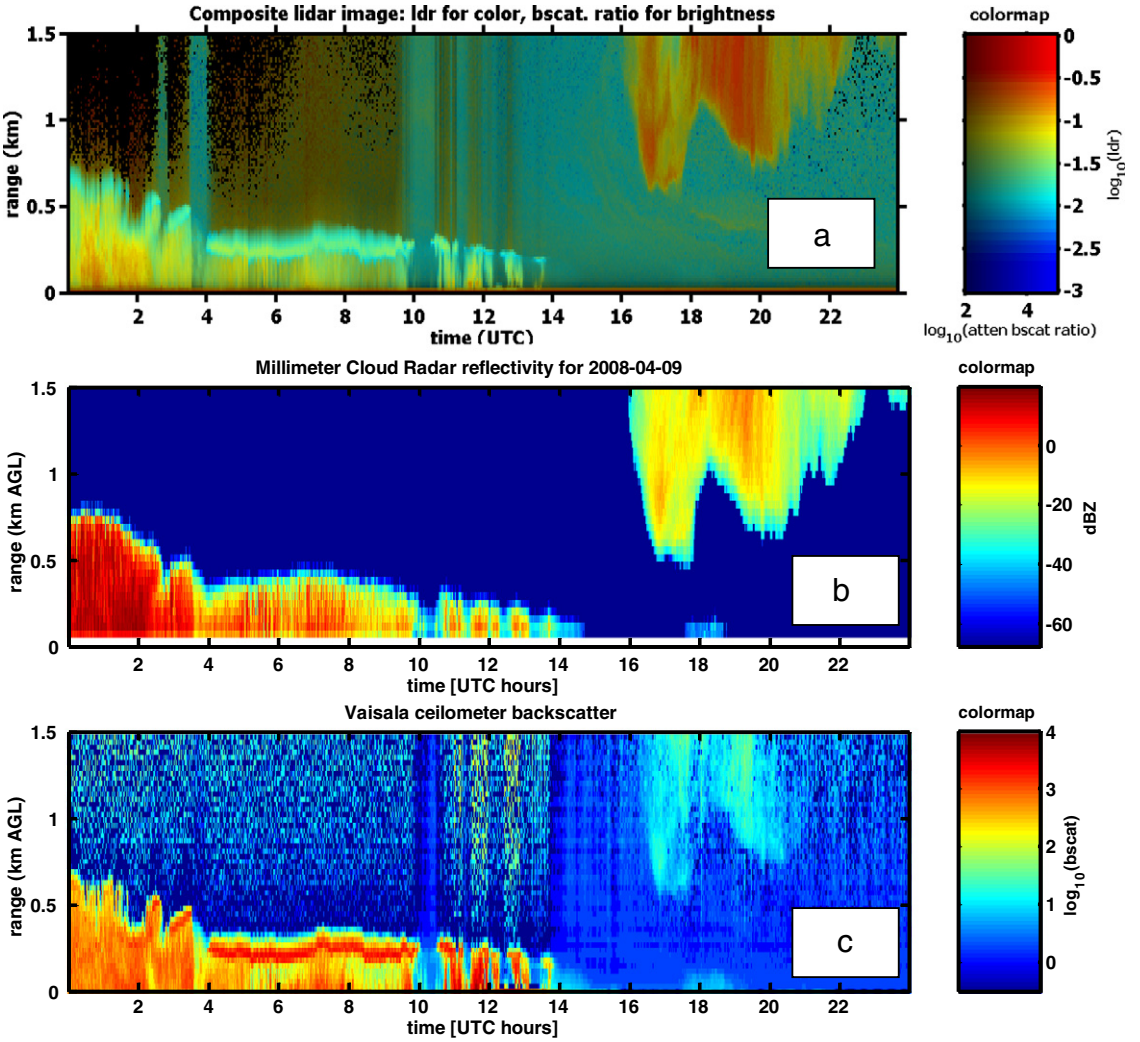

Fig. 9. Time-height cross sections of backscattering ratio for micro pulse lidar (MPL), reflectivity for mm cloud radar, and backscattering for the Vaisala ceilometer are shown in (a), (b), and (c), respectively, for an ice fog event took place over DOE NSA site during FRAM-IF project on April 9, 2008.

are quite useful for monitoring ice fog when there are no overlapping cloud layers present. Sophisticated approaches for determining cloud phase (Pavolonis, 2010a, 2010b) and the probability of clouds with hazardous low ceilings (Calvert and Pavolonis, 2011) were developed in preparation for the next generation Geostationary Operational Environmental Satellite (GOES-R) Advanced Baseline Imager (Schmit et al., 2001, 2005, 2008; Menzel and Purdom, 1994). On Meteosat Spinning-Enhanced Visible and Infrared Imager (SEVIRI) cloud phase determination (Cermak and Bendix, 2008) and explicit cloud base determination for liquid–water clouds (Cermak and Bendix, 2011) are possible due to the good spectral resolution. The algorithms utilize a series of infrared-based spectral and spatial tests to determine cloud phase (liquid water, supercooled water, mixed phase, ice) and cloud height. In lieu of brightness temperature differences, effective absorption optical depth ratios are used in the spectral tests. As shown in Pavolonis (2010a), effective absorption optical depth ratios, allow for improved sensitivity to cloud microphysics, especially for optically thin clouds. Using the MODerate Resolution Imaging Spectroradiometer (MODIS), the GOES-R cloud phase algorithm was tested during the FRAM-IF (Gultepe et al., 2014). Figures 8a and 8b show the false color image and cloud phase from a nighttime overpass of *Aqua* MODIS on 18 December 2010.

The cloud particle phase results show mixed phase and ice clouds at the vicinity of Yellowknife, which is consistent with surface observations. The low cloud base identification algorithm determines the probability that the cloud base (ceiling) is lower than 914 m above ground level (AGL) and the probability that the cloud base is 305 m AGL. These conditions correspond to the Marginal Visual Flight Rules (MVFR) and Instrument Flight Rules (IFR) categories, respectively. A naïve Bayesian classifier (e.g. Kossin and Sitowski, 2008) is used to objectively determine the probability of MVFR and IFR conditions. Both satellite and NWP model data are used as predictors and ceilometer based surface observations of cloud ceiling are used to train the classifier. Figures 8a and 8d show the probability of MVFR cloud ceilings and IFR cloud ceilings, respectively, that are consistent FRAM-IF measurements. Additional methods for satellites to detect and characterize fog and low clouds can be found in Gultepe et al. (2007), Wetzel et al. (1996), Ellrod (2007), Lee et al. (1997), Cermak and Bendix (2007), and Bendix (2005). Overall, satellite measurements show promise for

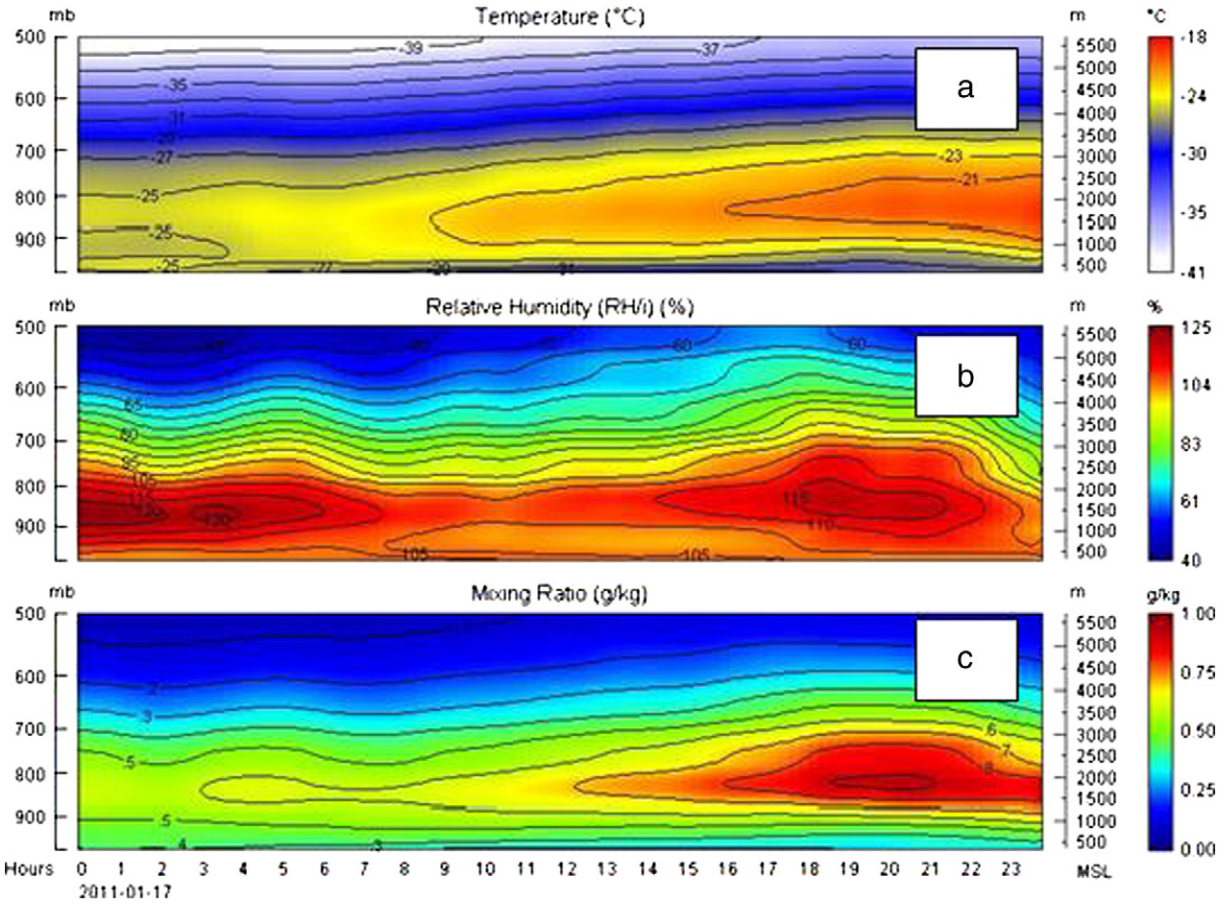

Fig. 10. Time-height cross-section of T (a), relative humidity with respect to ice (RH_i) (b), and Q_v (c) measurements from PMWR platform during January 17, 2011ice fog event over the Yellowknife International Airport.

detecting and characterizing ice fog. However, coverage over the Arctic regions is limited at the moment, and geostationary satellite observations suffer from reduced resolution in these areas (Cermak and Bendix, 2007).

7.2. Lidar, radar, and ceilometer based monitoring

Ice fog measurements can be obtained using a lidar (Light Detection and Ranging), a millimeter cloud radar, or a ceilometer. Backscattering from ice fog crystal particles is related to lidar transmitted wavelength, ice crystal surface area, and number of ice crystals. Sassen (1991) and Sassen and Zhu (2009) stated that ice crystal microphysical properties can be obtained using a polarization lidar and provided an extensive review on lidar capabilities to discriminate ice particle shape. Backscattering (β) of lidar transmitted radiation reflects the volumetric properties of ice crystal number concentration spectra and their mass density. If liquid clouds exist, a lidar beam cannot be used to detect high level ice clouds. Fig. 9a shows a vertical profile of backscatter ratio (k) and linear depolarization ratio (LDR) through ice clouds collected during FRAM-IF project in Barrow, Alaska, USA, which was part of the Department Of Energy (DOE) Indirect and Semi-Direct Aerosol Campaign (ISDAC) project (Flynn et al., 2007; Lindeman et al., 2011). The maximum ß and LDR (Fig. 9a) are about 4.3 and -2, respectively, and that indicates the high concentration of N_i at the ice fog top.

The DOE Millimeter-wavelength Cloud Radar (MMCR-8 mm; 35 GHz) reflectivity that corresponds to the lidar backscatter (Fig. 9a) is shown in Fig. 9b. Details of DOE MMCR can be found in Matrosov (2010). The cloud radar reflectivity (Z) is approximately between 10 dBZ and −10 dBZ for the same ice fog layer. The Z values likely represent larger particles because of their 6th power of the particle size. Latest studies on mm cloud radar applications (Haeffelin et al., 2010; Uematsu et al., 2005; Hamazu et al., 2003; Mead et al., 1989; Boers et al., 2013) have also studied fog distribution and its microphysical characteristics for nowcasting applications. These suggest that MMCR can be easily adapted for ice fog studies because of larger particle sizes during ice fog events compared to warm fog droplets.

The ceilometer uses a wavelength at 0.905 μm with low energy power to measure the cloud and fog macro-physical characteristics (Gultepe et al., 2009, 2014; Haeffelin et al., 2010) e.g. fog or cloud base at the different levels (Fig. 9c). Its operation is similar to RADAR; however, CL51 uses shorter wavelengths (ultraviolet to infrared) which permits the detection of smaller particles. If clouds are optically thick, a ceilometer cannot detect high level clouds. Vaisala CL-31 ceilometer backscatter image (Fig. 9c) corresponding to lidar returns suggests that its measurements can be used for ice fog detection. It provides a backscattering profile range of 0 to 10 km with a reporting resolution being about 10 m. The device fires 110 ns laser pulses at a repetition rate of 6.5 kHz and average power of the laser is 19.5 mW with a beam divergence of ~0.02° (Nowak et al. 2008). The β values for the same ice fog event (Fig. 9c) were about 2–4 km^{-1}.

7.3. PMWR based monitoring

The measurements from a Radiometrics profiling microwave radiometer (PMWR) (Gultepe et al., 2014; Ware et al., 2013, 2003; Cadeddu et al., 2009, Cadeddu et al., 2013; Cimini et al., 2010; Bianco et al., 2005; Solheim et al., 1998) can be used to retrieve T, RH_i, and Q_v (Fig. 10; LWC not shown). Below 3 km level where T was between −20 and −35 °C (Fig. 10a), relatively high RH_i values were observed (Fig. 9b). Ice fog was observed below about 700 mb where Q_v (Fig. 10c) reached up to 0.8 g kg^{-1}. Very close to the earth surface, Q_v was about 0.30 g kg^{-1} when ice fog Vis was about 1 km observed by FD12p.

Integration of satellite based retrievals of ice fog microphysical parameters with surface based sensors including a lidar, cloud radar, ceilometer, and microwave radiometer, as well as surface in-situ fog sensors e.g. a fog and visibility sensor (FD12p) can be used to improve the prediction of the fog micro and macro properties. This type of integration systems is being developed at the Environment Canada, Cloud Physics and Severe Weather Section, and used in the Arctic field projects.

8. Summary and future challenges

Ice fog is an important meteorological event occurring at low temperatures and quite often specifically at high elevations and northern high latitudes. Ice fog occurs very often when temperatures go down below −15 °C. In fact, IN can be found at T as high as −8 °C (Gultepe et al., 2008).

When T is very low, RH_i can easily be saturated with respect to ice with less moisture that leads to formation of ice fog crystals. Ice fog is strongly related to frost formation, and it might be more dangerous to aircraft than snow because of the stronger surface adhesion compared to snow particles at cold temperatures. Its impact on aviation and local weather and climate can be very significant (flight delays and severe icing hazard). Ice fog may also lead to frost formation but frost formation may not always be related to ice fog occurrence. In addition, the combination of ice fog and frost conditions may compromise power lines, leading to disruptions in electrical energy distribution.

Ice fog crystals can be as small as 5–10 μm, and usually have sizes less than 200 μm. Depending on their shape and density; ice crystals can be suspended in the air for a long time and may generate a very low PR (<0.01 mm h^{-1}) compared to light snow conditions. They may play an important role in controlling heat loss to the sky compared to the clear air conditions and cooling dependent on ice crystal spectral, physical, and optical properties. The following conclusions can be drawn from the present work:

- Ice fog Vis can be obtained from IWC and N_i that are derived prognostically from a forecast model. Models usually get N_i less than 100 L^{-1} based on microphysical parameterizations obtained from the aircraft observations; therefore, its prediction becomes questionable and N_i needs to be adjusted for specific environmental conditions.
- Ice fog crystal number concentration can be more than 1000 L^{-1} and IWC can be less than 0.005 g m^{-3}.
- Visibility measurements can be highly variable and a strong function of both N_i and IWC, and also particle shape.
- Present weather sensors are not calibrated at cold temperatures, and their optical properties may not represent the conditions at cold temperatures. Particle types and visibility obtained from the visibility sensor measurements should be

used cautiously.

- A better understanding of ice fog formation can also be used to improve the algorithms developed for numerical modeling studies of the ice clouds.
- Accurate prediction of ice fog Vis and IWC, and frost conditions can be used advantageously to help plan for the use of aircraft de-icing fluids in northern latitudes.
- Satellite based detection and nowcasting of ice fog events over cold climatic regions can be done if future operational satellites can be launched such as the PCW (Polar Communication and Weather) satellite (Kidder et al., 1990). Currently, operational satellites do not cover short time and space scales over the Arctic regions.
- Detailed ice fog 3D modeling work can be a major step to improve its prediction. This type of work is currently in the progress (Bott et al., 1990).
- Flying in the northern latitudes is more hazardous than in the mid-latitudes, and weather (particularly reduced visibility) is a major factor in the increased risk of aviation accidents. The per capita rate of aviation related fatalities in the northern regions can be up to 18 times higher than these for mid-latitudes.

Overall, the observations and numerical model simulations need to be improved for better prediction of ice fog events and understand how it impacts aviation, transportation, climate, and the hydro-meteorological cycle. It is believed that ice fog studies will be a major step to improving our understanding and forecasting of Arctic cold cloud systems and their effect on climate change.

Acknowledgments

Funding for this work was provided by the Canadian National Search and Rescue Secretariat (SAR) and Environment Canada. The authors would like to thank Dr. Flynn for providing the DOE MPL and ceilometer measurements and images, and US DOE for providing partial funding for FRAM-IF project (Grant DE-FG02-08ER64554).

References

Baker, B., Lawson, R.P., 2006. Improvement in determination of ice water content from two-dimensional particle imagery. Part I: image-to-mass relationships. J. Appl. Meteorol. Climatol. 45, 1282–1290.

Bendix, J., Thies, Boris, Cermak, Jan, Nauß, Thomas, 2005. Ground fog detection from space based on MODIS daytime data—a feasibility study. Weather Forecast. 20, 989–1005.

Benjamin, S.G., Devenyi, D., Weygandt, S.S., Brundage, K.J., Brown, J.M., Grell, G.A., Kim, D., Schwartz, B.E., Smirnova, T.G., Smith, T.L., Manikin, G.S., 2004. An hourly assimilation/forecast cycle: the RUC. Mon. Weather Rev. 132, 495–518.

Benson, C.S., 1965. Ice fog: low temperature air pollution defined with Fairbanks, Alaska as type locality. Geoph. Inst. Rept., UAG R-173. CRREL Res. Report. 121.

Benson, C.S., Rogers, G.W., 1965. Alaskan air pollution—the nature of ice fog and its development and settlement implications. Proc. Of the 16th AAAS Alaskan Sci. Conf., Juneau, pp. 233–245.

Bergot, T., Guedalia, D., 1994. Numerical forecasting of radiation fog. Part I: numerical model and sensitivity tests. Mon. Weather Rev. 122, 1218–1230.

Bergot, T., Terradellas, E., Cuxart, J., Mira, A., Liechti, O., Mueller, M., Nielsen, N.W., 2007. Intercomparison of single-column numerical models for the prediction of radiation fog. J. Appl. Meteorol. Climatol. 46, 504–521.

Bianco, Laura, Cimini, Domenico, Marzano, Frank S., Ware, Randolph, 2005. Combining microwave radiometer and wind profiler radar measurements for high-resolution atmospheric humidity profiling. J. Atmos. Ocean. Technol. 22, 949–965.

Boers, R., Klein Baltink, H., Hemink, H.J., Bosveld, F.C., Moerman, M., 2013. Ground-based observations and modeling of the visibility and radar reflectivity in a radiation fog layer. J. Atmos. Ocean. Technol. 30, 288–300.

Bott, A., Sievers, U., Zdunkowski, W., 1990. A radiation fog model with a detailed treatment of the interaction between radiative transfer and fog microphysics. J. Atmos. Sci. 47, 2153–2166.

Bowling, S.A., Ohtake, T., Benson, C.S., 1968. Winter pressure systems and ice fog in Fairbanks, Alaska. J. Appl. Meteorol. 7, 961–968.

Cadeddu, M., Turner, D., Liljegren, J., 2009. A neural network for real-time retrievals of PWV and LWP from Arctic millimeter-wave ground-based observations. IEEE Trans. Geosci. Remote Sens. 47 (7). http://dx.doi.org/10.1109/TGRS.2009.2013205.

Cadeddu, M.P., Liljegren, J.C., Turner, D.D., 2013. The atmospheric radiation measurement (ARM) program network of microwave radiometers: instrumentation, data, and retrievals. Atmos. Meas. Tech. 6, 2359–2372.

Calvert, C., Pavolonis, M.J., 2011. GOES-R Advanced Baseline Imager (ABI) Algorithm Theoretical Basis Document for Fog and Low Cloud Detection, Version 2.0. (67 pp.) .

Cermak, J., Bendix, J., 2007. Dynamical nighttime fog/low stratus detection based on Meteosat SEVIRI data — a feasibility study. Pure Appl. Geophys. 164, 1179–1192. http://dx.doi.org/10.1007/s00024-007-0213-8.

Cermak, J., Bendix, J., 2008. A novel approach to fog/low stratus detection using Meteosat 8 data. Atmos. Res. 87 (3–4), 279–292. http://dx.doi.org/10.1016/j.atmosres.2007.11.009.

Cermak, J., Bendix, J., 2011. Detecting ground fog from space—a microphysics-based approach. Int. J. Remote Sens. http://dx.doi.org/10.1080/0143116YY. 1-27.

Cimini, D., Campos, E., Ware, R., Albers, S., Giuliani, G., Oreamuno, J., Joe, P., Koch, S.E., Cober, S., Westwater, E., 2010. Thermodynamic atmospheric profiling during the 2010 Winter Olympics using ground-based microwave radiometry. IEEE Trans. Geosci. Remote Sens. 49, 12,4959–12,4969.

Côté, J., Gravel, S., Méthot, A., Patoine, A., Roch, M., Staniforth, A., 1998. The operational CMC-MRB Global Environmental Multiscale (GEM) model. Part I: design considerations and formulation. Mon. Weather Rev. 126, 1373–1395.

Curry, J.A., Meyers, F.G., Radke, L.F., Brock, C.A., Ebert, E.E., 1990. Occurrence and characteristics of lower tropospheric ice crystals in the Arctic. Int. J. Climatol. 10, 749–764.

DeMott, Paul J., Meyers, Michael P., Cotton, William R., 1994. Parameterization and impact of ice initiation processes relevant to numerical model simulations of cirrus clouds. J. Atmos. Sci. 51, 77–90.

Ellrod, G.P., Gultepe, I., 2007. Inferring low cloud base heights at night for aviation using satellite infrared and surface temperature data. J. of Pure and Applied Geophy. Vol. 164, 1193–1205.

Ferrier, B.S., Jin, Y., Lin, Y., Black, T., Rogers, E., DiMego, G., 2002. Implementation of a new grid-scale cloud and precipitation scheme in the NCEP Eta model. Preprints, 15th Conf. on Numerical Weather Prediction, San Antonio, TX, Amer. Meteor. Soc., 10.1.

Field, P.R., Heymsfield, A.J., Bansemer, A., 2006. Shattering and particle interarrival times measured by optical array probes in ice clouds. J. Atmos. Ocean. Technol. 23, 1357–1371.

Flynn, C.J., Mendoza, A., Zheng, Y., Mathur, S., 2007. Novel polarization-sensitive micropulse lidar measurement technique. Opt. Express 15 (6), 2785–2790.

Girard, E., Blanchet, J.P., 2001. Microphysical parameterization of arctic diamond dust, ice fog, and thin stratus for climate models. J. Atmos. Sci. 58, 1181–1198.

Glickman, T., 2000. Glossary of Meteorology, 2nd Ed. Amer. Meteor. Soc., 855 (Boston, MA, 565 pp).

Gotaas, Y., Benson, C.S., 1965. The effect of suspended ice crystals on radiative cooling. J. Appl. Meteorol. 4, 446–453.

Gultepe, I., Isaac, G.A., 2002. The effects of air-mass origin on Arctic cloud microphysical parameters during FIRE.ACE. J. Geophys. Res. Oceans 107 (C10), SHE 4-1–4-12.

Gultepe, I., Isaac, G.A., Cober, S.G., 2001. Ice crystal number concentration versus temperature for climate studies. Int. J. Climatol. 21, 1281–1302.

Gultepe, I., Isaac, G., Williams, A., Marcotte, D., Strawbridge, K., 2003. Turbulent heat fluxes over leads and polynyas and their effect on Arctic clouds during FIRE-ACE: aircraft observations for April 1998. Atmos. Ocean 41 (1), 15–34.

Gultepe, I., et al., 2007a. Fog research: a review of past achievements and future perspectives. Pure Appl. Geophys. 164, 1121–1159.

Gultepe, I., Pagowski, M., Reid, J., 2007b. Using surface data to validate a satellite based fog detection scheme. Weather Forecast. 22, 444–456.

Gultepe, I., Minnis, P., Milbrandt, J., Cober, S.G., Nguyen, L., Flynn, C., Hansen, B., 2008. The Fog Remote Sensing and Modeling (FRAM) field project: visibility analysis and remote sensing of fog. In: Feltz, Wayne F., Murray, John J. (Eds.), Remote sensing applications for aviation weather hazard detection and decision support. Proceedings of SPIE, vol. 7088-2. SPIE, San Diego, CA. ISBN: 9780819473080 (12 pages, 204 pp).

Gultepe, I., Pearson, G., Milbrandt, J.A., Hansen, B., Platnick, S., Taylor, P., Gordon, M., Oakley, J.P., Cober, S.G., 2009. The fog remote sensing and modeling (FRAM) field project. Bull. Am. Meteorol. Soc. 90, 341–359.

Gultepe, I., Kuhn, T., Pavolonis, M., Calver, C., Gurka, J., Isaac, G.A., Heymsfield, A.J., Liu, P., Zhou, B., Ware, R., Sloan, J., Milbrandt, J., Bernstein, B., 2012. Ice fog (pogonip) and frost in Arctic during FRAM-Ice Fog project: aviation and nowcasting applications. The 16th International Conference on Clouds and Precipitation (ICCP), 30 July–3 August 2012, Leipzig, Germany. Extended abstract in CD.

Gultepe, I., Kuhn, T., Pavolonis, M., Calvert, C., Gurka, J., Heymsfield, A.J., Liu, P.S.K., Zhou, B., Ware, R., Ferrier, B., Milbrandt, J., Bernstein, B., 2014. Ice Fog in Arctic During FRAM–Ice Fog Project: Aviation and Nowcasting Applications. Bulletin of Amer. Met. Soc. 95, 211–226.

Gultepe, I., Kuhn, T., Pavolonis, M., Calvert, C., Gurka, J., Heymsfield, A.J., Liu, P.S.K., Zhou, B., Ware, R., Ferrier, B., Milbrandt, J., Bernstein, B., 2014. Ice fog in Arctic during FRAM-ICE for project: aviation and nowcasting applications. Bull. Am. Meteorol. Soc 95, 211–226.

Haeffelin, M., Coauthors, 2010. PARISFOG: shedding new light on fog physical processes. Bull. Am. Meteorol. Soc. 91, 767–783.

Hamazu, K., Hashiguchi, Hiroyuki, Wakayama, Toshio, Matsuda, Tomoya, Doviak, Richard J., Fukao, Shoichiro, 2003. A 35-GHz scanning doppler radar for fog observations. J. Atmos. Ocean. Technol. 20, 972–986.

Heymsfield, A.J., Thompson, G., Morrison, H., Bansemer, A., Rasmussen, R.M., Minnis, P., Wang, Z., Zhang, D., 2011. Formation and spread of aircraft-induced holes in clouds. Science, AAAS 333, 77–81.

Hobbs, P.V., 1965. The aggregation of ice particles in clouds and fogs at low temperatures. J. Atmos. Sci. 22, 296–300.

Jaecker-Voirol, A., Mirabel, P., 1989. Heteromolecular nucleation in the sulfuric acid-water system. Atmos. Environ. 23, 2053–2057.

Kidder, S.Q., Vonder Haar, T.H., 1990. On the use of satellites in Molniya orbits for meteorological observation of middle and high latitudes. J. Atmos. Ocean. Technol. 7, 517–522.

Kim, C.K., Stuefer, M., Schmitt, C.G., Heymsfield, A.J., Thompson, G., 2014. A numerical modeling of ice fog in Interior Alaska using weather research and forecasting model. Pure Appl. Geophys. http://dx.doi.org/10.1007/s00024-013-0766-7.

Koeing, L.R., 1970. Numerical modeling of ice deposition. J. Atmos. Sci. 28, 226–237.

Koop, T., Luo, B., Tsias, A., Peter, T., 2000. Water activity as the determinant for homogeneous ice nucleation in aqueous solutions. Lett. Nat. 404, 611–614.

Korolev, A.V., Isaac, G.A., 2003. Roundness and aspect ratio of particles in ice clouds. J. Atmos. Sci. 60, 1795–1808.

Kossin, J.P., Sitkowski, M., 2008. An objective model for identifying secondary eyewall formation in hurricanes. Mon. Weather Rev. 137, 876–892.

Kumai, 1964. A study of ice fog and ice-fog splintering nuclei at Fairbanks, Alaska. U.S. Army Cold Regions Research and Engineering Lab. (USA CRREL) Research Report (150 pp.).

Langmuir, I., Schaefer, V.J., Vonnegut, B., Maynard, K., Smith-Johannsen, R., Blanchard, D., Falconer, R.E., 1948. Final reports, Project Cirrus, RL140. General Electric Res. Lab. Req 21190 with the Depart. of the Army Project: 3-99-07-022 (119 pp.).

Lawson, R.P., 2011. Effects of ice particles shattering on optical cloud particle probes. Atmos. Meas. Tech. Discuss. 4, 939–968.

Lawson, R.P., Baker, B.A., Zmarzly, P., O'Connor, D., Mo, Q., Gayet, J.F., Schherbakov, V., 2006a. Microphysical and optical properties of atmospheric ice crystals at south pole station. J. Appl. Meteorol. Climatol. 45, 1505–1524.

Lawson, R.P., O'Connor, D., Zmarzly, P., Weaver, K., Kaker, B., Mo, Q., Jonsson, H., 2006b. The 2D-S (stereo) probe: design and preliminary tests of a new airborne, high-speed, high-resolution particle imaging probe. J. Atmos. Ocean. Technol. 23, 1462–1477.

Lawson, R.P., Baker, B.A., Zmarzly, P., O'Connor, D., Mo, Q., Gayet, J.-F., Shcherbakov, V., 2006c. Microphysical and optical properties of atmospheric ice crystals at south pole station. J. Appl. Meteorol. Climatol. 45, 1505–1524.

Lawson, R.P., Jensen, E., Mitchell, D., Baker, B., Mo, Q., Pilson, B., 2010. Microphysical and radiative properties of tropical clouds investigated in TC4 and NAMM. J. Geophys. Res. 115, D00J08.

Lee, T.F., Turk, F.J., Richardson, K., 1997. Stratus and fog products using GOES-8-9 3.9-μm data. Weather Forecast. 12, 664–677.

Lindeman, J., Boybeyi, Z., Gultepe, I., 2011. The aerosol semi-direct effect during a polluted case of the ISDAC field campaign. The aerosol semi-direct effect during a polluted case of the ISDAC field campaign. JGR Atmos. 116, D00T10. http://dx.doi.org/10.1029/2011JD015649.

Ludlam, F.H., 1956. Fall-streak holes. Weather 11, 89–90.

Matrosov, S.Y., 2010. Synergetic use of millimeter- and centimeter-wavelength radars for retrievals of cloud and rainfall parameters. Atmos. Chem. Phys. 10, 3321–3331.

Mead, J.B., Mcintosh, Robert E., Vandemark, Douglas, Swift, Calvin T., 1989. Remote sensing of clouds and fog with a 1.4-mm radar. J. Atmos. Ocean. Technol. 6, 1090–1097.

Menzel, W.P., Purdom, J.F.W., 1994. Introducing GOES-I: the first of a new generation of geostationary operational environmental satellites. Bull. Am. Meteorol. Soc. 75, 757–781.

Meyers, M.P., DeMott, P.J., Cotton, W.R., 1992. New primary ice-nucleation parameterizations in an explicit cloud model. J. Appl. Meteorol. 31, 708–721.

Milbrandt, J.A., Yau, M.K., 2005a. A multi-moment bulk microphysics parameterization. Part I: analysis of the role of the spectral shape parameter. J. Atmos. Sci. 62, 3051–3064.

Milbrandt, J.A., Yau, M.K., 2005b. A multimoment bulk microphysics parameterization. part II: a proposed three-moment closure and scheme description. J. Atmos. Sci. 62, 3065–3081.

Morrison, Hugh, Milbrandt, Jason, 2011. Comparison of two-moment bulk microphysics schemes in idealized supercell thunderstorm simulations. Mon. Weather Rev. 139, 1103–1130.

Morrison, H., Curry, J.A., Khvorostyanov, V.I., 2005. A new double-moment microphysics parameterization for application in cloud and climate models. Part I: description. J. Atmos. Sci. 62, 1665–1677.

Mueller, M.D., Masbou, M., Bott, A., 2010. Three-dimensional fog forecasting in complex terrain. Q. J. R. Meteorolog. Soc. 136, 2189–2202.

Murray, F.W., 1967. On the computation of saturation vapor pressure. J. Appl. Meteorol. 6, 203–204.

Nowak, D., Ruffieux, D., Agnew, J.L., Vuilleumier, L., 2008. Detection of fog and low cloud boundaries with ground-based remote sensing systems. J. Atmos. Ocean. Technol. 25, 1357–1368.

Nygaard, K., Egil, Bjørn, Kristjánsson, Jón Egill, Makkonen, Lasse, 2011. Prediction of in-cloud icing conditions at ground level using the WRF model. J. Appl. Meteorol. Climatol. 50, 2445–2459.

Ohtake, T., 1967. Alaskan ice fog. Proc. Intern. Conf. Physics of Snow and Ice, Part I, Hokkaido University, Sapporo, Japan, pp. 105–118.

Ohtake, T., Huffman, P.J., 1969. Visual range in ice fog. J. Appl. Meteorol. 8, 499–501.

Pavolonis, M.J., 2010a. Advances in extracting cloud composition information from spaceborne infrared radiances: a robust alternative to brightness temperatures part I: theory. J. Appl. Meteorol. Climatol. 49, 1992–2012.

Pavolonis, M.J., 2010b. GOES-R Advanced Baseline Imager (ABI) Algorithm Theoretical Basis Document for Cloud Type and Cloud Phase, Version 2.0, available from NOAA, Madison, Wisconsin (86 pp.).

Robinson, E., Thuman, W.C., Wiggins, E.J., 1957. Ice fog as a problem of air pollution in the Arctic. Arctic 10, 88–104.

Rogers, E., DiMego, G., Black, T., Ek, M., Ferrier, B., Gayno, G., Janjic, Z., Lin, Y., Pyle, M., Wong, V., Wu, W.-S., Carley, J., 2009. The NCEP North American mesoscale modeling system: recent changes and future plans. Proc. 23rd Conference on Weather Analysis and Forecasting/19th Conference on Numerical Weather Prediction, American Meteorological Society, Omaha, NE.

Sassen, K., 1991. The polarization lidar technique for cloud research: a review and current assessment. Bull. Am. Meteorol. Soc. 72, 1848–1866.

Sassen, K., Zhu, J., 2009. A global survey of CALIPSO linear depolarization ratios in ice clouds: initial findings. J. Geophys. Res. 114, D00H07.

Schmit, T.J., Prins, E.M., Schreiner, A.J., Gurka, J.J., 2001. Introducing the GOES-M imager. Natl. Wea. Assoc. Digest 25, 28–37.

Schmit, T.J., Gunshor, M.M., Menzel, W.P., Li, J., Bachmeier, S., Gurka, J.J., 2005. Introducing the next-generation Advanced Baseline Imager (ABI) on GOES-R. Bull. Am. Meteorol. Soc. 86, 1079–1096.

Schmit, T.J., Li, J., Gurka, J.J., Goldberg, M.D., Schrab, K.J., Li, Jinlong, Feltz, W.F., 2008. The GOES-R Advanced Baseline Imager and the continuation of current sounder products. J. Appl. Meteorol. 47, 2696–2711.

Solheim, F., Godwin, J., Westwater, E., Han, Y., Keihm, S., Marsh, K., Ware, R., 1998. Radiometric profiling of temperature, water vapor, and liquid water using various inversion methods. Radio Sci. 33, 393–404.

Stoelinga, T.G., Warner, T.T., 1999. Non-hydrostatic, mesobeta-scale model simulations of cloud ceiling and visibility for an east coast winter precipitation event. J. Appl. Meteorol. 38, 385–404.

Szyrmer, W., Zawadzki, I., 1997. Biogenix and anthropogenic sources of ice forming-ice nuclei: a review. Bull. Am. Meteorol. Soc. 78, 209–227.

Thompson, G., Rasmussen, Roy M., Manning, Kevin, 2004. Explicit forecasts of winter precipitation using an improved bulk microphysics scheme. Part I: description and sensitivity analysis. Mon. Weather Rev. 132, 519–542.

Thompson, G., Field, Paul R., Rasmussen, Roy M., Hall, William D., 2008. Explicit forecasts of winter precipitation using an improved bulk microphysics scheme. Part II: implementation of a new snow parameterization. Mon. Weather Rev. 136, 5095–5115.

Thuman, W.C., Robinson, E., 1954. Studies of Alaskan ice-fog particles. J. Meteorol. 11, 151–156.

Uematsu, A., Hashiguchi, Hiroyuki, Teshiba, Michihiro, Tanaka, Hisamichi, Hirashima, Koichi, Fukao, Shoichiro, 2005. Moving cellular structure of fog echoes obtained with a millimeter-wave scanning doppler radar at Kushiro, Japan. J. Appl. Meteorol. 44, 1260–1273.

Velde, D.V.I.R., Steeneveld, G.J., Schreur, B.G.J.W., Holtslag, A.M., 2010. Modeling and forecasting the onset and duration of severe radiation fog under frost conditions. Mon. Weather Rev. 138, 4237–4253.

Ware, R., Carpenter, R., Guldner, J., Liljegren, J., Nehrkorn, T., Solheim, F., Vandenberghe, F., 2003. A multichannel radiometric profiler of temperature, humidity, and cloud liquid. Radio Sci. 38 (4), 8079. http://dx.doi.org/10.1029/2002RS002856.

Ware, R., Cimini, D., Campos, E., Giuliani, G., Albers, S., Nelson, M., Koch, S.E., Joe, P., Cober, S., 2013. Thermodynamic and liquid profiling during the 2010 Winter Olympics. Atmos. Res. 278–290.

Wendler, G., 1969. Heat balance studies an ice fog period in Fairbanks, Alaska. Mon. Weather Rev. 7, 512–520.

Wetzel, M.A., Borys, R.D., Xu, L.E., 1996. Satellite microphysical retrievals for land-based fog with validation by balloon profiling. J. Appl. Meteorol. 35, 810–829.

Wexler, H., 1936. Cooling in the lower atmosphere and structure of polar continental air. Mon. Weather Rev. 64, 122–136.

Wexler, H., 1941. Observations of nocturnal radiation at Fairbanks, Alaska, and Frago, North Dakota. Mon. Weather Rev. 46 (21 pp.).

Woodley, W.L., Henderson, T.J., Vonnegut, B., Gordon, G., Breidenthal, R., Holle, S.M., 1991. Aircraft-produced ice particles (APIPs) in supercooled clouds and the probable mechanism for their production. J. Appl. Meteorol. 30, 1469–1489.

Young, C.K., 1974. The role of contact nucleation in ice phase initiation in clouds. J. Atmos. Sci. 31, 768–776.

Zelenyuk, A., Imre, D.G., 2005. Single particle laser ablation time-of-flight mass spectrometer: an introduction to SPLAT. Aerosol Sci. Technol. 39 (6), 554–568.

Zhou, B., 2011. Introduction to a new fog diagnostic scheme. NCEP Office Note 466, U.S. Dept. of Commerce, NOAA, National Weather Service, NCEP p. 32.

Zhou, B., Du, J., 2010. Fog prediction from a multi-model mesoscale ensemble prediction system. Weather Forecast. 25, 303–322.

Zhou, B., Ferrier, B.S., 2008. Asymptotic analysis of equilibrium in radiation fog. J. Appl. Meteorol. Climatol. 47, 1704–1722.